

Development of a Three-Dimensional Meso- γ Primitive Equation Model: Katabatic Winds Simulation in the Area of Terra Nova Bay, Antarctica

HUBERT GALLÉE AND GUY SCHAYES

Institut d'Astronomie et de Géophysique G. Lemaître, Université Catholique de Louvain, Louvain-la-neuve, Belgium

(Manuscript received 20 October 1992, in final form 20 September 1993)

ABSTRACT

The spatial evolution of Antarctic katabatic winds in the area of Terra Nova Bay is examined using the three-dimensional version of the Université Catholique de Louvain—Modèle Atmosphérique Régional (UCL—MAR) mesoscale primitive equation models. The ability of the model to replicate classical linear mountain wave simulations is verified. Then, three-dimensional experiments are performed for the terrain configuration of Terra Nova (Ross Sea coastal zone) using different horizontal resolutions (5, 10, and 20 km). The model converges for resolutions lower than 10 km. Results are in qualitative agreement with available observations and previous modeling work. Strong katabatic winds are simulated with a jet over Terra Nova Bay. The model seems able to initiate the mesocyclonic activity in the Ross Sea due to the katabatic circulation.

1. Introduction

The katabatic wind is a gravity-driven atmospheric current that is forced by the cooling of air adjacent to a sloped surface. It is observed all around the world and called “glacier” or “gravity” wind (Mather and Miller 1967). It is generally classified as a mesoscale phenomenon. The most remarkable exception to this rule arises when the length scale of the slope becomes as large as the scale of a continent and when the surface cooling conditions required for the production of a strong sloped inversion are satisfied. This is the case at least for Greenland and Antarctica, especially during the long polar night. For such situations the downslope-induced wind reaches a stormy character and this is perhaps the most remarkable climatic feature that has been observed on polar ice caps (Parish 1988).

Model studies (Parish and Bromwich 1987, 1991) have shown that Antarctic katabatic winds are very strong in topographic confluence zones because of the large supply of negatively buoyant air. This is particularly true in Adélie Land and in the area of Terra Nova Bay, where extensive observations of this phenomenon have been done (e.g., André et al. 1986; Baldi et al. 1990, respectively).

Evolution of the katabatic winds in the Antarctic coastal zone has also been studied. For example, sudden decays of katabatic winds before they pass the coastline have been observed in Adélie Land (Pettré

and André 1991). On the other hand, it has been inferred from thermal infrared satellite imagery that strong katabatic winds in the area of Terra Nova Bay can sometimes propagate horizontally for over hundreds of kilometers after passing the coastline (Bromwich 1989). It is believed that the presence of the stable, annually recurring Terra Nova Bay polynya (water area free of ice) is due to strong, persistent katabatic winds that blow far offshore (Kurtz and Bromwich 1985). Coastal polynyas like that of Terra Nova Bay are of particular importance, because of the strong energy exchanges between ocean and atmosphere occurring in these areas.

Another example of the importance of katabatic winds in the Antarctic coastal zone is its activating role in the formation of mesocyclones in the coastal zone of the Ross Sea. Mesocyclones seem to play a key role in the dynamics of the Southern Hemisphere polar regions. It has been found at McMurdo Station on Ross Island that the mesocyclonic maximum activity that occurs in fall coincides with the climatological maximum of estimated precipitation (Bromwich 1991).

In a previous paper (Gallée and Schayes 1992), the katabatic wind evolution on idealized slopes representative of the coastal area of Antarctica has been analyzed. Some ideas about the kind of physical mechanisms that are responsible for the persistence or the weakening of katabatic wind in such an area were given.

One purpose of this paper is to discuss katabatic wind simulations on more realistic slopes, using the three-dimensional version of the Université Catholique de Louvain—Modèle Atmosphérique Régional (UCL—MAR) meso- γ model. Katabatic winds over the com-

Corresponding author address: Dr. Hubert Gallée, Institut d'Astronomie et de Géophysique G. Lemaître, 2, Chemin du cyclotron 1348, Louvain-la-neuve, Belgium.

plex topography of the region of Terra Nova (Ross Sea coastal zone) will be simulated. The results will be compared with available observations and previous simulations, with particular attention to the katabatic wind evolution over the ice-sheet slopes. The study will be restricted to the case of a pure katabatic wind event where the ocean is covered with sea ice. Polar night will be assumed. Because of the simplicity of the initial conditions and external forcing used, the conclusions of this study must be considered as rather qualitative. The model will be described in section 2 and verified in section 3. In section 4, the results of katabatic wind simulations are presented. Conclusions are drawn in section 5.

2. The model

a. Equations of the atmospheric model

The atmosphere is simulated with a mesoscale primitive equation model in which the full continuity equation is taken into account. To express the surface boundary conditions in a way that is as easy as possible and to allow a wide variety of applications, the pressure ratio σ coordinate is used:

$$\sigma = \frac{p - p_t}{p_*}, \quad (1)$$

where p is pressure, p_t refers to the pressure at the top of the model (set equal to 50 hPa), p_s is the surface pressure, and $p_* = p_s - p_t$.

The use of the pressure ratio is preferable to the height ratio because this allows a more accurate integration of the hydrostatic equation, using the finite-difference approximation (S. Tanrikulu, J. Carroll, and M. Liu, 1991, personal communication). Horizontal equations for momentum are therefore

$$\begin{aligned} \frac{\partial u}{\partial t} = & -u \frac{\partial u}{\partial x} - v \frac{\partial u}{\partial y} - \dot{\sigma} \frac{\partial u}{\partial \sigma} \\ & + f(v - v_g) - \left. \frac{\partial \phi}{\partial x} \right|_p + F_u \end{aligned} \quad (2)$$

$$\begin{aligned} \frac{\partial v}{\partial t} = & -u \frac{\partial v}{\partial x} - v \frac{\partial v}{\partial y} - \dot{\sigma} \frac{\partial v}{\partial \sigma} \\ & - f(u - u_g) - \left. \frac{\partial \phi}{\partial y} \right|_p + F_v, \end{aligned} \quad (3)$$

where x and y are the horizontal axes; t is time, u , v , and $\dot{\sigma}$ are the x , y , and σ components of the mean wind, respectively; f is the Coriolis parameter; $\mathbf{V}_g = (u_g, v_g)$ is the geostrophic wind; $(-fv_g, fu_g)$ represents the synoptic-scale pressure gradient force in the σ -coordinate system; R_a is the perfect gas constant for dry air; T is the mean air temperature; $\phi = gz$ is the sum of the basic-state geopotential and the mesoscale geopotential perturbation; g is gravity; z is altitude; and $|_p$ means

that the terms representing the mesoscale pressure gradient force $[-(\partial\phi/\partial x), -(\partial\phi/\partial y)]$ are calculated on an isobaric surface.

Note that in our model the initial temperature field is assumed to depend on z only and that the initial mean sea level surface pressure is constant, even with a non-zero geostrophic wind. Consequently, the synoptic-scale perturbation is not included in ϕ . This simplification of the large-scale dynamics seems acceptable to us because horizontal temperature gradients are typically of the order of $1 \text{ K } (10 \text{ km})^{-1}$ at the meso- γ scale, while the neglected synoptic-scale temperature gradients are at least one order of magnitude smaller, except perhaps in synoptic-scale fronts.

The divergences of the turbulent momentum fluxes are F_u and F_v (prime quantities are turbulent fluctuations):

$$F_u = -\frac{1}{p_*} \frac{\partial(p_* \overline{u'u'})}{\partial x} - \frac{1}{p_*} \frac{\partial(p_* \overline{v'u'})}{\partial y} - \frac{\partial(\overline{\dot{\sigma}'u'})}{\partial \sigma} \quad (4)$$

$$F_v = -\frac{1}{p_*} \frac{\partial(p_* \overline{u'v'})}{\partial x} - \frac{1}{p_*} \frac{\partial(p_* \overline{v'v'})}{\partial y} - \frac{\partial(\overline{\dot{\sigma}'v'})}{\partial \sigma}, \quad (5)$$

where the overbar indicates the time average. It must be pointed out that to preserve simplicity the overbar is avoided except for the turbulent fluxes.

The vertical momentum equation is approximated by the hydrostatic equilibrium:

$$\frac{\partial \phi}{\partial(T/\theta)} = -C_p \theta (1 + 0.85q), \quad (6)$$

where

$$\theta = T \left(\frac{p_0}{p} \right)^\kappa \quad (7)$$

is the definition of potential temperature, $p_0 = 1000$ hPa, $\kappa = R_a/C_p$, C_p is the specific heat at constant pressure for dry air, and q is the specific humidity.

The equation of state for humid air as a perfect gas is given by

$$p = \rho R_a T (1 + 0.608q). \quad (8)$$

The full continuity equation is used and is expressed through the time tendency equation for p_* :

$$\frac{\partial p_*}{\partial t} = - \int_0^1 \left[\frac{\partial(p_* u)}{\partial x} + \frac{\partial(p_* v)}{\partial y} \right] d\sigma, \quad (9)$$

from which the vertical velocity $\dot{\sigma}$ in σ coordinates can be computed:

$$\begin{aligned} \dot{\sigma} = & \frac{1}{p_*} \left\{ \sigma \int_0^1 \left[\frac{\partial}{\partial x} (p_* u) + \frac{\partial}{\partial y} (p_* v) \right] d\sigma \right. \\ & \left. - \int_0^\sigma \left[\frac{\partial}{\partial x} (p_* u) + \frac{\partial}{\partial y} (p_* v) \right] d\sigma \right\}. \end{aligned} \quad (10)$$

The thermodynamic energy equation is

$$\frac{\partial \theta}{\partial t} = -u \frac{\partial \theta}{\partial x} - v \frac{\partial \theta}{\partial y} - \dot{\sigma} \frac{\partial \theta}{\partial \sigma} + \frac{\partial R_{\text{IR}}}{\partial \sigma} + F_{\theta}, \quad (11)$$

where R_{IR} is the infrared radiative heat flux (Sasamori 1968) and

$$F_{\theta} = -\frac{1}{p_*} \frac{\partial(p_* \overline{u' \theta'})}{\partial x} - \frac{1}{p_*} \frac{\partial(p_* \overline{v' \theta'})}{\partial y} - \frac{\partial(\overline{\dot{\sigma}' \theta'})}{\partial \sigma} \quad (12)$$

is the divergence of the turbulent heat flux.

The specific humidity conservation is expressed with the following equation:

$$\frac{\partial q}{\partial t} = -u \frac{\partial q}{\partial x} - v \frac{\partial q}{\partial y} - \dot{\sigma} \frac{\partial q}{\partial \sigma} + F_q, \quad (13)$$

where

$$F_q = -\frac{1}{p_*} \frac{\partial(p_* \overline{u' q'})}{\partial x} - \frac{1}{p_*} \frac{\partial(p_* \overline{v' q'})}{\partial y} - \frac{\partial(\overline{\dot{\sigma}' q'})}{\partial \sigma} \quad (14)$$

is the divergence of the turbulent moisture flux.

Equations (2), (3), (6), (8)–(11), and (13) form a system of eight equations for eight unknowns, u , v , $\dot{\sigma}$, ϕ , p_* , ρ , θ , and q ; p and T can be obtained from the definitions (1) and (7) of σ and θ , respectively; and the turbulent fluxes introduced in (4), (5), (12), and (14) will be parameterized.

It should be noted that a two-dimensional version of this set of equations is easily obtained by eliminating all the terms containing a derivative with respect to y (see Gallée and Schayes 1992; Alpert et al. 1982).

b. Upper and lower boundary conditions

The boundary conditions at the top of the model, where $p = p_i$ ($\sigma = 0$), are

$$\dot{\sigma} = 0 \quad (15)$$

$$\frac{\partial u}{\partial \sigma} = \frac{\partial v}{\partial \sigma} = 0 \quad (16)$$

$$\theta = \theta_{\text{obs}} \quad (17)$$

$$q = q_{\text{obs}} \quad (18)$$

To minimize reflection from the upper boundary, we use a viscous damping layer at the top of the domain, similar to that used by Klemp and Lilly (1978), to absorb vertically propagating waves. This absorbing layer takes the following form:

$$K_t = \begin{cases} 0, & k \geq s \\ K_{\text{max}} \frac{\sigma_s - \sigma_k}{\sigma_s}, & k < s, \end{cases} \quad (19)$$

where K_t is added to the horizontal eddy exchange coefficient (see below), $k = 1$ refers to the highest level of the model, and s is equal to the total number of levels divided by a factor of 3. The nondimensional value $K'_{\text{max}} = K_{\text{max}}(\Delta t / \Delta x^2)$ is 0.1.

The boundary conditions at the surface ($\sigma = 1$) are

$$u, v = 0 \quad (20)$$

$$T = T_s(t) \quad (21)$$

$$q = q_s(T_s), \quad (22)$$

where T_s is the predicted air surface temperature in function of time t (see below) and q_s is the saturation specific humidity corresponding to the air surface temperature T_s . This last choice is made because in our simulations the surface is assumed to be covered by snow.

c. Lateral boundary conditions

To help suppress spurious boundary reflections, the following radiation conditions are used:

$$\frac{\partial \psi}{\partial t} + c \frac{\partial \psi}{\partial x} = 0, \quad (23)$$

where $\psi = u, v, \theta$, or q and c is the wave velocity. This scheme has been introduced by Orlanski (1976) and discussed later by Miller and Thorpe (1981). The third-order-accurate-in-space formulation of Miller and Thorpe (1981) is used for determining c .

d. Parameterization of subgrid-scale fluxes

For each variable $\psi = u, v, \theta$, or q , the expression of the subgrid-scale fluxes is of the form

$$F_{\psi} = -\frac{1}{p_*} \frac{\partial(p_* \overline{u' \psi'})}{\partial x} - \frac{1}{p_*} \frac{\partial(p_* \overline{v' \psi'})}{\partial y} - \frac{\partial(\overline{\dot{\sigma}' \psi'})}{\partial \sigma} \quad (24)$$

Alpert and Neumann (1984) have obtained simple relationships between vertical subgrid-scale fluxes in the rectangular coordinate system and in the σ system. To do this, the two following approximations have been made.

(i) Assuming that the local variation of the geopotential is small, the expression for the vertical velocity in the rectangular coordinate system is

$$w = \frac{dz}{dt} \approx \frac{1}{g} u \frac{\partial \phi}{\partial x} + \frac{1}{g} v \frac{\partial \phi}{\partial y} - \frac{p_* \dot{\sigma}}{\rho g} \quad (25)$$

(ii) It is presumed that in regions of topography the terms $|\partial \bar{\phi} / \partial x_i|$ are larger than $|\partial \phi' / \partial x_i|$, with $x_i = x, y$. And one gets

$$\overline{\psi' \dot{\sigma}'} = \frac{\rho g}{p_*} \left(-\overline{\psi' w'} + \overline{\psi' u'} \frac{\partial \bar{z}}{\partial x} + \overline{\psi' v'} \frac{\partial \bar{z}}{\partial y} \right) \quad (26)$$

An eddy diffusivity first-order closure is used to ap-

proximate the horizontal subgrid-scale flux where K_H is the eddy exchange coefficient. This could be done in the rectangular coordinate system and then transformed into the σ system (Alpert and Neumann 1984):

$$\overline{\psi' u'} = -K_H \left. \frac{\partial \bar{\psi}}{\partial x} \right|_z = -K_H \left(\left. \frac{\partial \bar{\psi}}{\partial x} \right|_\sigma + \frac{\partial \sigma}{\partial x} \frac{\partial \bar{\psi}}{\partial \sigma} \right) \quad (27)$$

$$\overline{\psi' v'} = -K_H \left. \frac{\partial \bar{\psi}}{\partial y} \right|_z = -K_H \left(\left. \frac{\partial \bar{\psi}}{\partial y} \right|_\sigma + \frac{\partial \sigma}{\partial y} \frac{\partial \bar{\psi}}{\partial \sigma} \right). \quad (28)$$

The eddy exchange coefficient K_H parameterization is adapted from Smagorinsky (1963):

$$K_H = K_t + (k_H l_H)^2 \left[\frac{1}{2} \left(\frac{\partial v}{\partial x} + \frac{\partial u}{\partial y} \right)^2 + \left(\frac{\partial u}{\partial x} \right)^2 + \left(\frac{\partial v}{\partial y} \right)^2 \right]^{1/2}, \quad (29)$$

where $l_H = \Delta x$ is the assumed mixing length and k_H is a dimensionless constant, whose value ranges between 0.2 and 0.4 (Tag et al. 1979); the value $k_H = 0.4$ has been taken; K_t is different from zero only in the absorbing layer (see 19). After some algebra, one gets from (24), (26), (27), and (28)

$$\begin{aligned} F_\psi = & \underbrace{\frac{1}{p_*} \frac{\partial}{\partial x} \left(p_* K_H \frac{\partial \bar{\psi}}{\partial x} \right)}_{A_{\psi,x}} + \underbrace{\frac{1}{p_*} \frac{\partial}{\partial y} \left(p_* K_H \frac{\partial \bar{\psi}}{\partial y} \right)}_{A_{\psi,y}} + \underbrace{\frac{g}{p_*} \frac{\partial}{\partial x} \left(\rho \alpha K_H \frac{\partial \bar{\psi}}{\partial \sigma} \right)}_{B_{\psi,x}} \\ & + \underbrace{\frac{g}{p_*} \frac{\partial}{\partial y} \left(\rho \beta K_H \frac{\partial \bar{\psi}}{\partial \sigma} \right)}_{B_{\psi,y}} + \underbrace{\frac{g}{p_*} \frac{\partial}{\partial \sigma} \left(\rho \alpha K_H \frac{\partial \bar{\psi}}{\partial x} \right)}_{C_{\psi,x}} + \underbrace{\frac{g}{p_*} \frac{\partial}{\partial \sigma} \left(\rho \beta K_H \frac{\partial \bar{\psi}}{\partial y} \right)}_{C_{\psi,y}} \\ & + \underbrace{\frac{\partial}{\partial \sigma} \left[\left(\frac{\rho g}{p_*} \alpha \right)^2 K_H \frac{\partial \bar{\psi}}{\partial \sigma} \right]}_{D_{\psi,x}} + \underbrace{\frac{\partial}{\partial \sigma} \left[\left(\frac{\rho g}{p_*} \beta \right)^2 K_H \frac{\partial \bar{\psi}}{\partial \sigma} \right]}_{D_{\psi,y}} - \underbrace{\frac{\partial}{\partial \sigma} \left(\frac{\rho g}{p_*} \overline{\psi' w'} \right)}_{E_\psi}, \quad (30) \end{aligned}$$

where $\alpha = \partial \bar{z} / \partial x$ and $\beta = \partial \bar{z} / \partial y$ (the x and y slope components of the σ surface, respectively). Terms $A_{\psi,x}$ and $A_{\psi,y}$ are the diffusion terms on σ surfaces. Term E_ψ is the divergence of the vertical turbulent flux. Terms $B_{\psi,x}$, $B_{\psi,y}$, $C_{\psi,x}$, $C_{\psi,y}$, $D_{\psi,x}$, and $D_{\psi,y}$ are correction terms. The form of relations (30) is very similar to that of Alpert and Neumann (1984) except that it allows K_H to be variable in space and time. For simplicity, the use of the correction terms will be referenced hereafter as the Alpert–Neumann correction. It should be mentioned here that such correction holds only when the grid aspect ratio is not too large. Otherwise, the horizontal mixing length chosen in the parameterization (29) of K_H is not appropriate when using it with vertical gradients, as is done in the correction terms $B_{\psi,x}$, $B_{\psi,y}$, $D_{\psi,x}$, and $D_{\psi,y}$.

The impact of the correction terms on the simulation of katabatic winds in the area of Terra Nova Bay will be tested for several horizontal grid sizes (see below).

1) VERTICAL TURBULENT DIFFUSION ABOVE THE SURFACE LAYER

The parameterization of turbulence above the surface layer is done by expressing the term $\overline{\psi' w'}$ found

in the development of (4), (5), (12), and (14) by the classical Austausch exchange formulation, and one gets

$$E_\psi = + \frac{g^2}{p_*^2} \frac{\partial}{\partial \sigma} \left(\rho^2 K_\psi \frac{\partial \bar{\psi}}{\partial \sigma} \right), \quad (31)$$

where $K_\psi = K_z$ for $\psi = u, v$ is the vertical turbulent diffusion coefficient for momentum, and $K_\psi = K_{zh}$ for $\psi = \theta, q$ is the vertical turbulent diffusion coefficient for heat. They are expressed as follows:

$$K_z = l^2 \left| \frac{\Delta \bar{V}}{\Delta z} \right| F(\text{Ri}) \quad (32)$$

$$K_{zh} = l^2 \left| \frac{\Delta \bar{V}}{\Delta z} \right| F_h(\text{Ri}), \quad (33)$$

where

$$\begin{aligned} l &= \frac{kz}{1 + (kz/\lambda)} \\ \frac{\Delta \bar{V}}{\Delta z} &= \left[\left(\frac{\partial \bar{u}}{\partial z} \right)^2 + \left(\frac{\partial \bar{v}}{\partial z} \right)^2 \right]^{1/2} \\ \text{Ri} &= \frac{g}{\theta} \frac{(\partial \bar{\theta} / \partial z)}{(\Delta \bar{V} / \Delta z)^2} \end{aligned}$$

are the mixing length, the wind shear, and the Richardson number, respectively. The functions $F(\text{Ri})$ and $F_h(\text{Ri})$ of the Richardson number are given by Louis (1979). The value of λ is chosen to be 10 m.

2) VERTICAL TURBULENT DIFFUSION IN THE SURFACE LAYER

The parameterization of turbulence will be different for the surface layer. The turbulent fluxes in the surface layer may be assumed constant, and it is possible to get from the observations a good parameterization of them.

The formulation is given by Businger (1973), who uses the scaling variables u_* , θ_* , q_* , and the Monin–Obukhov length L

$$u_*^2 = -\overline{V'w'} \quad (34)$$

$$-\overline{u'w'} = \frac{\bar{u}}{\bar{V}} u_*^2 \quad (35)$$

$$-\overline{v'w'} = \frac{\bar{v}}{\bar{V}} u_*^2 \quad (36)$$

$$-\overline{\theta'w'} = u_* \theta_* \quad (37)$$

$$-\overline{q'w'} = u_* q_* \quad (38)$$

$$L = -\frac{\bar{\theta} u_*^2}{kg \theta_*}, \quad (39)$$

where $k = 0.4$ is the von Kármán constant, w is the vertical velocity in z coordinates, and $V = (u^2 + v^2)^{1/2}$. Using universal functions and taking into account the roughness length z_0 of the iced surface taken as 10^{-4} m, the scaling variables are obtained through the values of the corresponding variables at the 10-m height (Businger 1973), providing the relationships between $u_{10\text{ m}}$ and u_* , $\Delta q = q_{10\text{ m}} - q_s(T_s)$ and q_* , $\Delta \theta = \theta_{10\text{ m}} - \theta_s$ and θ_* , where θ_s is the potential temperature at the surface. It is therefore possible to use these relations and (34)–(39) in order to determine the contribution of the turbulent diffusions F_u , F_v , F_θ , and F_q in the surface layer.

In the model, the first layer is assumed to be the surface layer. In the present paper, katabatic wind simulations have been performed taking 10 m as the depth of the first layer. In fact, this may be too deep for the katabatic situation, especially over gentle slope. Assuming a too deep surface layer could lead to an overestimation of the air temperature near the surface. Indeed, because of the strong temperature inversion, the deeper the layer, the warmer the mean layer temperature. This could cause an inhibition of the katabatic force, particularly over gentle slope, and result in an underestimation of the wind speed, the friction velocity, and the (downward) sensible heat flux. Consequently, surface temperature decrease would be overestimated, amplifying spuriously the temperature difference between the surface and the surface layer. We

have verified the possible occurrence of this shortcoming by testing the simulated katabatic wind sensitivity to the surface-layer depth. Sensitivity experiments have been done with the two-dimensional version of the model over a parabolic topography representing Antarctica. These experiments have shown that the simulated katabatic wind intensity converges for surface-layer depths smaller or equal to 10 m.

e. The numerical scheme of the model

The model is discretized on a nonstaggered grid, using high-order differencing schemes on high spatial resolution. This efficient method has been developed by Purser and Leslie (1988).

The numerical scheme used to solve (2), (3), (11), and (13) for u , v , θ , and q is based on splitting techniques (i.e., Marchuk 1974). The contribution of the pressure gradient force to the horizontal momentum equations is achieved by using a numerical scheme centered, second-order-accurate in time (leap frog) and centered, fourth-order-accurate in space. For the advection, a semi-Lagrangian scheme is used. This scheme is based on the cubic-spline interpolation technique (e.g., Pielke 1984) and has been improved by Seibert and Morariu (1991).

To avoid the generation of short-scale spurious waves on σ surfaces in the three-dimensional version of the model, the selective two-dimensional low-pass filter proposed by Raymond and Garder (1988) is used for the variables u , v , θ , and q . For the two-dimensional version of the model, the Long et al. (1978) filter is used. The weighting parameter of the filter is equal to 0.004. With such a value, the contribution of the filter is much less than horizontal diffusion except for the $2\Delta x$ and $2\Delta y$ waves, which are completely removed. Model sensitivity to the value of δ is quite negligible when $\delta \leq 0.01$. Taking $\delta = 0.002$, for example, modifies the wind speed by less than 0.03 m s^{-1} except locally where weak numerical instability occurs. Values of δ larger than 0.01 speed up the convergence of the model but smooth the solution, particularly in the coastal area.

The conservation equation (9) for p_* is solved by using a numerical scheme centered, second-order-accurate in time (leap frog) and centered, fourth-order-accurate in space. We prefer to filter the difference $p_* - p_{*,0}$ rather than p_* , where $p_{*,0}$ is the value of p_* at the beginning of the integration. This avoids spurious mass loss and a subsequent generation of instability where the slope varies.

Because spurious mass loss could occur in the model especially through the lateral boundaries, the correction proposed by Yan and Anthes (1987) is used, namely, by restoring the model average \bar{p}_* of p_* to its initial value $\bar{p}_{*,0}$. This is achieved by adding at each horizontal grid point the difference $K_r(\bar{p}_{*,0} - \bar{p}_*)$, where $K_r = 1.157 \times 10^{-5} \text{ s}^{-1}$.

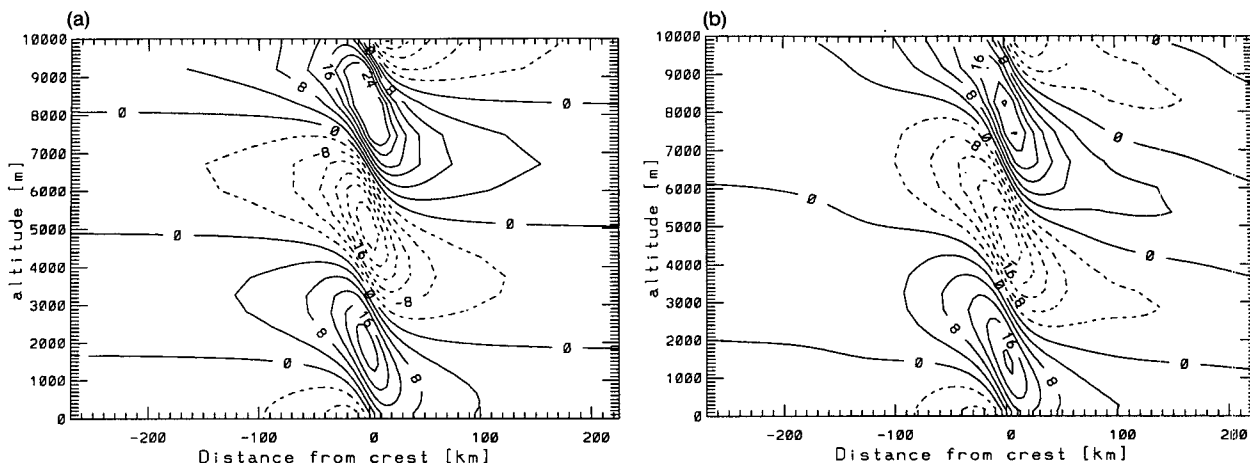


FIG. 1. Perturbation velocity from (a) the linear hydrostatic solution for a 1-km-high mountain; (b) the numerical simulation for a 1-m-high mountain (amplified by a factor of 1000).

The horizontal grid spacing of the model is regular: for the two-dimensional mountain wave simulations, we have chosen $\Delta x = 5$ km, while for the three-dimensional simulations, $\Delta x = 5, 10$, and 20 km. Vertical discretization is irregular to get more σ levels close to the surface. For the katabatic winds simulations, the initial heights of the σ levels are $z = 10, 20, 40, 78, 152, 295, 560, 1034, 1833, 3082, 4870, 7217, 10\,082, 13\,420$, and $17\,233$ m. The time step is such that the Courant–Friedrichs–Lewy criterion is satisfied for the fast Lamb waves. For example, $\Delta t = 10$ s was adopted when $\Delta x = 5$ km.

f. The surface model

Ground surface temperature is predicted from the force-restore slab model of Deardorff (1978):

$$\frac{\partial T_s}{\partial t} = -C_1 \frac{H_A}{\rho_s c_s d_1} - C_2 \frac{T_s - T_2}{\tau_1}, \quad (40)$$

with $C_1 = 3.72$, $C_2 = 7.4$, H_A (positive upward) is the sum of the heat fluxes coming from the atmosphere and absorbed at the ice-sheet surface. The surface parameters are those of the snow, which is assumed to cover the sea ice and the continental ice during the Antarctic winter: the specific mass— $\rho_s = 330 \text{ kg m}^{-3}$; the heat capacity— $c_s = 2 \times 10^3 \text{ J kg}^{-1} \text{ K}^{-1}$; the thermal diffusivity— $\kappa_s = 0.27 \times 10^{-6} \text{ m}^2 \text{ s}^{-1}$; the depth reached by the diurnal temperature wave— $d_1 = (\kappa_s \tau_1)^{1/2} = 0.15$ m; and the length of the day— $\tau_1 = 86\,400$ s. Although the polar night is assumed, the choice of the day length for τ_1 accelerates the model convergence. Finally, T_2 is the mean temperature of the ice and is assumed to be the average of T_s over the previous 24 hours.

3. Model verification

In this section one verifies the ability of the model to simulate linear waves over an idealized mountain by

comparing the model simulation to the analytical solution. The turbulence scheme has also been tested by simulating a simple free-convective mixed layer. This second verification is discussed at the end of the section.

Linear mountain waves over bell-shaped mountains have been studied and analytical solutions are known (e.g., Queney 1948). Although the numerical model is not linear, it should produce a steady solution that closely approximates the analytical solution when the height of the mountain is very small. A “linear” experiment has been performed with the model by using a 1-m-high mountain of 20-km half-width. The atmosphere is initially isothermal (250 K) and the initial wind is from the west at 20 m s^{-1} . For this experiment, subgrid-scale fluxes are not included, the numerical filter is not used, and the Coriolis parameter is chosen to be zero. A free-slip condition is used at the lower boundary of the model.

The perturbation velocity and potential temperature fields are compared in Fig. 1 and Fig. 2, respectively, with the results of the analytical solution for a 1-km-high mountain. The numerical model results have been amplified by a factor of 1000 for visualization purposes and are shown after 12 h of model time. The model agrees quite well with the linear solution, and in particular, unwanted small wavelength features are not generated. This very stable numerical behavior of the model is of particular importance, because it would not require strong numerical damping that could preclude an accurate simulation of drainage flows.

Because turbulence is important for katabatic flow, the turbulence scheme has been verified by simulating a simple free-convective mixed layer, with no winds and a constant surface heat flux of 100 W m^{-2} . A constant vertical lapse rate of 4°C km^{-1} was chosen as the initial condition. Results show that the heat flux profile is linearly decreasing with height but no negative value at the top of the

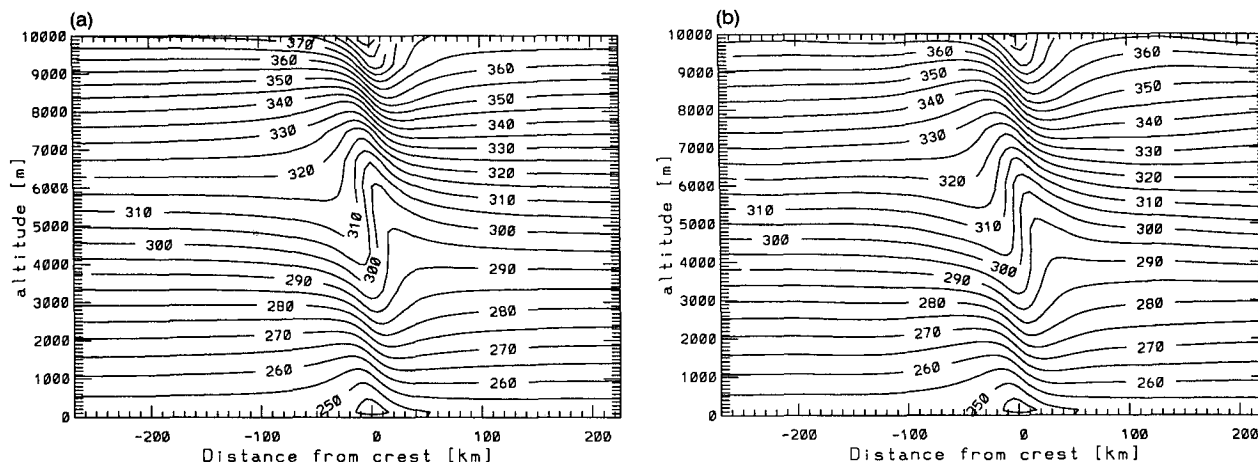


FIG. 2. As in Fig. 1 but for potential temperature.

mixed layer is simulated. This is due to the fact that we parameterize turbulence using a first-order small-eddy K theory, precluding the representation of the large eddies associated with the convective mixed layer.

4. Simulations of katabatic winds in the area of Terra Nova Bay

Terra Nova Bay (75°S, 164°E) is in the Ross Sea (see Fig. 3). This area is located downwind of a pronounced confluence region in the Antarctic interior wind field simulated by Parish and Bromwich (1987). Because in a confluence zone negatively buoyant air converges from a large interior section of the ice sheet, the supply of cold air to sustain katabatic winds blowing down the coastal marginal ice slopes is considerably enhanced (Parish 1984). This is why in the area of Terra Nova Bay the katabatic wind speed may be as large as 25 m s^{-1} (e.g., Parish and Bromwich 1989). In the present section we will describe simulations of this atmospheric circulation that have been done with our meso- γ atmospheric model.

The terrain topography is taken from the Drewry (1983) map (see Fig. 3). The total coverage of the model is up to the 50-hPa pressure level in the vertical and $650 \text{ km} \times 510 \text{ km}$ in the horizontal. The Terra Nova confluence zone is contained in the integration domain and is limited by mountains in the coastal area.

Simulations have been performed for polar night conditions. The initial vertical temperature profile is that observed by Schwerdtfeger (1984, his Fig. 6.9, p. 225, the Vostok sounding of July), with temperatures in the lowest level extrapolated downward from the temperature profile above the inversion. The geostrophic wind vector is chosen to be $\mathbf{V}_g = (0, 0)$.

a. Sensitivity to the grid size and Alpert–Neumann correction

Several katabatic winds simulations have been done to test the model sensitivity to the horizontal discreti-

zation and to the use of the Alpert–Neumann correction. Coarse horizontal resolution may impact the katabatic wind simulation by smoothing out the topography significantly (Bromwich et al. 1990) and by letting unresolved a larger amount of motion scales in the horizontal. These subgrid fluxes are parameterized using a first-order closure scheme, and the mixing length used is chosen to be the grid size [see (29)]. The consequence of a larger grid size is an enhanced horizontal diffusion. To avoid such problems, one has to define a sufficiently small horizontal grid size. Several horizon-

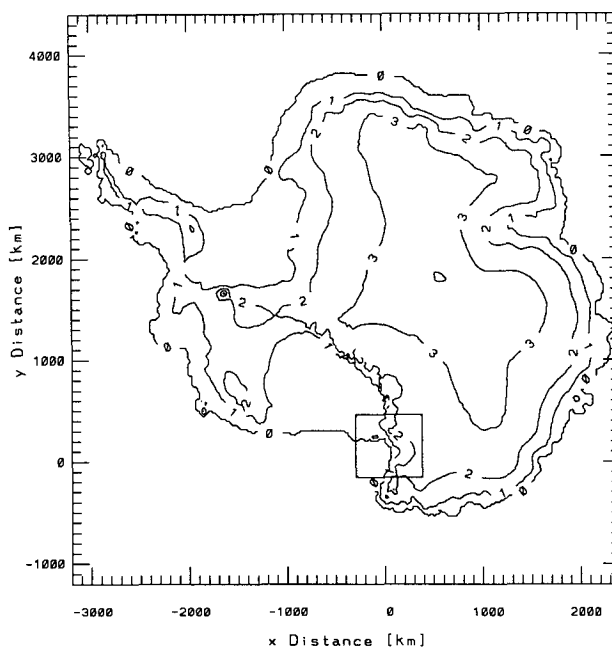


FIG. 3. The terrain topography of Antarctica (adapted from Drewry 1983) and the model domain located in the area of Terra Nova Bay. The contour interval is 1 km.

tal resolutions have been tested, namely, $\Delta x = 5, 10$, and 20 km.

Moreover, the Alpert–Neumann correction could also alter the results when coarse horizontal resolutions are used. Indeed, in this case the grid aspect ratio is large, so that this correction is not appropriate (see section 2.4). The impact of the Alpert–Neumann correction has been tested by removing the correction terms in (30).

The wind field obtained after 36-h simulation time is not far from its maximum. This was verified by continuing experiment N5 (see Table 1) until 38 h simulation time. These two extra hours contributed only to the 0.18 m s^{-1} increase in wind speed maximum at 10 m over the ground. The main results of the sensitivity experiments (i.e., wind maximum at the end of simulated hour 36) are summarized in Table 1. It can be seen that the model tends to converge for horizontal grid sizes less or equal to 10 km. The convergence is better when the Alpert–Neumann correction is not used. Despite this fact, the simulations N5 and H5, using a grid size $\Delta x = 5$ km, are comparable.

A closer comparison between the two experiments N5 and H5 can be done from their simulated wind norm at the first sigma level (10 m above the surface—see Figs. 4a and 4b, respectively). It can be seen in general that the use of the Alpert–Neumann correction slightly weakens the simulated katabatic flow. However, the main features of the circulation are quite comparable. In both experiments, the strongest winds are simulated around the 800-m surface elevation contour in the left side of the valley (looking downwind) and katabatic winds are simulated over the ocean, extending seaward up to several tens of kilometers. These winds are characterized by speeds up to 12 m s^{-1} at the coast. Over the ocean, katabatic winds are stronger in experiment N5. The simulated features N5 and H5 agree qualitatively with the observations (e.g., Bromwich 1989) and with previous modeling work (e.g., Bromwich et al. 1990). The katabatic wind speed is underestimated by roughly $20\%–30\%$, as compared with the observations. The main differences with the simulation of Bromwich et al. occur in other areas than the valley itself, where the simulated wind is significantly weaker in the present simulations. In conclusion, the model result is not sensitive to the use of the Alpert–Neumann correction.

b. Analysis of the N5 experiment

We will now analyze in detail experiment N5. The wind vectors are shown in Fig. 5 for the lowest sigma level of the model. Vectors whose norms are less than 1 m s^{-1} are not plotted. Over the plateau the wind is deflected to the left because of the Coriolis force. Convergence is simulated in the lower part of the valley, with enhanced wind speeds. In this area the wind direction is across the topography isolines. Strong wind blows at the left foot of the valley and propagates over

TABLE 1. Katabatic wind simulations in the area of Terra Nova, Antarctica. Sensitivity to the horizontal grid size used, with the correction of Alpert and Neumann (1984) or not. Maximum wind speed is given for the lowest sigma level of the model (approximately 10 m above the surface) after 36-h simulation time. The label of each experiment is given in parentheses.

Δx (km)	Wind norm (m s^{-1})	
	No correction	Horizontal correction
5	19.2 (N5)	19.6 (H5)
10	19.0 (N10)	18.8 (H10)
20	17.7 (N20)	17.2 (H20)

the ocean. The localization of these strong winds is consistent with the observation of a polynya in Terra Nova Bay during the winter months, which has been found to be forced by katabatic winds (Bromwich and Kurtz 1984). The simulated wind over the ocean is generally small, and some areas exist with wind speeds less than 1 m s^{-1} . This is simply explained by the fact that our simulation is started at rest (i.e., the large-scale forcing is absent), so that the katabatic stream has not yet reached these areas.

At sigma level 5 (approximately 150 m above the surface), the 6 m s^{-1} isotach (Fig. 6) almost coincides with the 2200-m surface elevation contour, as measured by Parish and Bromwich (1989). In the lower part of the valley, the wind speed reaches 16 m s^{-1} at the 1200-m surface elevation contour. This is comparable to what has been observed by Parish and Bromwich (1989) near the head of Reeves Glacier, at an altitude of 1200 m. Our model does not simulate the stronger wind speeds (up to $18\text{--}28 \text{ m s}^{-1}$) that were observed downstream along Reeves Glacier at this level.

It should be mentioned that the topography used to force the model is smoothed when compared to real topography, as can be inferred from the United States Geological Survey reconnaissance maps of the Antarctic coastal regions (e.g., Bromwich et al. 1990). In particular, the two-valley structure located in the coastal area of Terra Nova and shown by Bromwich et al. (1990) could strengthen the katabatic wind by an increased channeling effect. This two-valley structure is not described in the topography that was used in our simulations, so that channeling effects are slightly underestimated. This could partly explain some discrepancies between our simulation and the observations downstream from the 1200-m surface elevation contour. A more important point is that the synoptic forcing was absent in the model simulation and may be a significant factor in actual case studies. This problem is discussed at the end of section 4. In addition, the actual wind speeds themselves are not known with much spatial fidelity.

More precisely, Fig. 5 (displaying the wind vectors for the lowest sigma level of the model) shows distinct

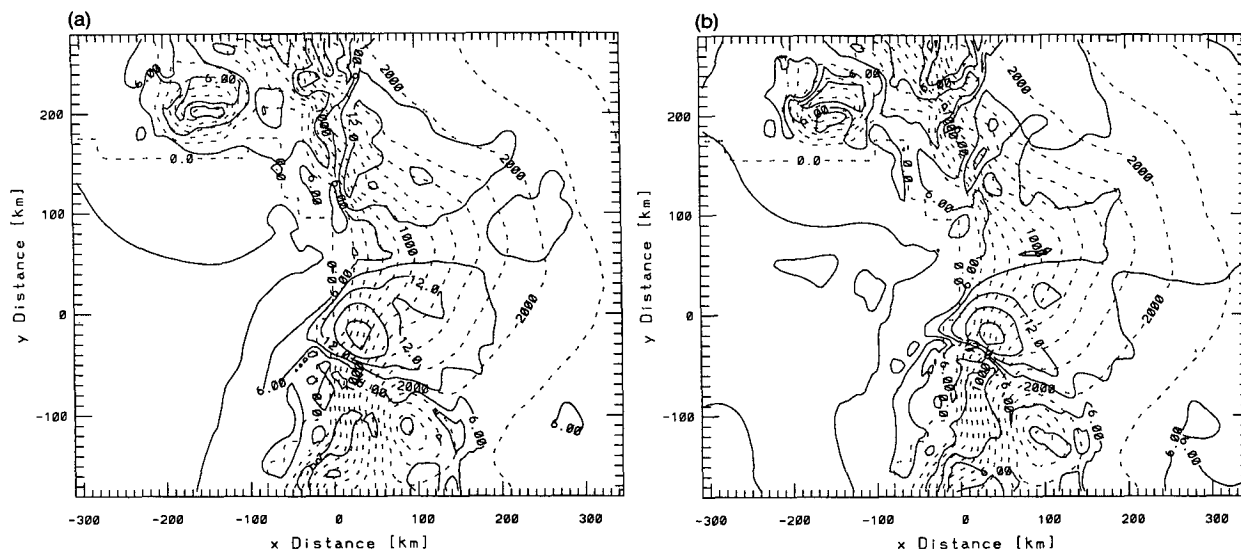


FIG. 4. Model katabatic wind isotachs after 36-h time integration for the lowest level of the model (10 m above the surface): (a) simulation N5 (without the Alpert-Neumann correction); (b) simulation H5 (with the Alpert-Neumann correction). The horizontal grid size used is 5 km for both experiments. The contour interval is 3 m s^{-1} . Ice-sheet elevation contours in (m, dashed) are also plotted. The contour interval is 200 m.

simulated wind patterns characterized by a local speed maximum and a relative directional constancy. For simplicity, these patterns are called jets in the following. One may find the jets J1 and J2 in the left side of the valley and the jet J3 coming from its right side; J1, J2, and J3 may also be inferred from the 12 m s^{-1} isotachs in Fig. 4a.

The leftmost jet J1 is the strongest and is characterized by strong lateral potential temperature gradients along the mountain. (See Fig. 7 displaying the potential temperatures for the lowest sigma level of the model.) The wind norm and wind vector are also characterized by strong lateral variations in this area. This is even more marked at higher levels—for example, for the third sigma level—and is due in our model to the to-

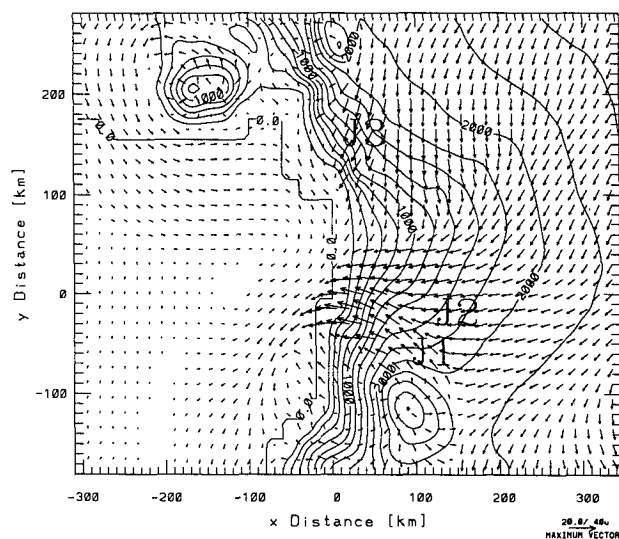


FIG. 5. Model katabatic wind vectors after 36-h time integration for the lowest level of the model (10 m above the surface), for simulation N5 (without the Alpert-Neumann correction). Ice-sheet elevation contours (m) are also plotted. Contour interval is 200 m. Vectors whose norms are less than 1 m s^{-1} are not plotted. Vectors are plotted every three grid points. The arrow length at the right bottom corner of the graph represents wind speed amounting to 20 m s^{-1} .

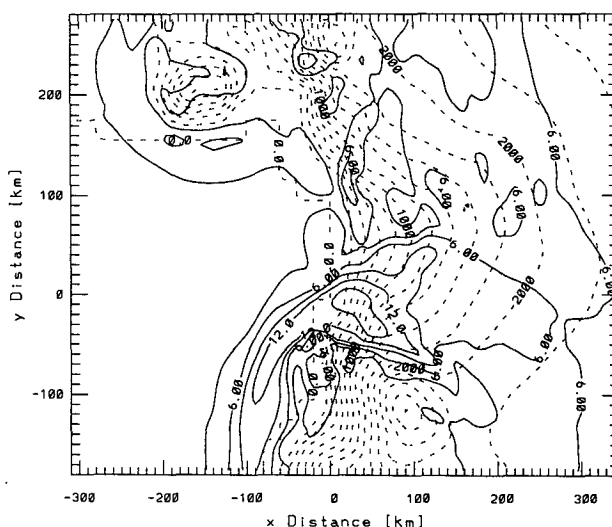


FIG. 6. Model katabatic wind isotachs after 36-h time integration for the fifth level of the model (150 m above the surface), for simulation N5 (without the Alpert-Neumann correction). The contour interval is 3 m s^{-1} . Ice-sheet elevation contours (m, dashed) are also plotted. The contour interval is 200 m.

jump. Figure 9 shows the vertical structure of the y component of the wind field in the plane $x = +10$ km of Fig. 5 for this katabatic jump. This vertical structure and that of potential temperature are very similar to those simulated by Gallée and Schayes (1992). Ascending air is also found in the area of the jump.

We will now analyze in detail the vertical structure of the left jets. Figure 10 shows the x component of the wind in the vertical plane $y = -20$ km of Fig. 5. The potential temperature distribution in the same vertical plane is shown in Fig. 11. These vertical cross sections allow us to have a look at the flow characteristics in the jet core.

The signature of the two left jets J1 and J2 can be found in Fig. 10. The jet J2 is the farthest from the coast with a maximum wind speed amounting to 14.4 m s^{-1} . The jet J1 begins at 120 km far from the coast. Its thickness is larger than that of jet J2. The maximum simulated wind speed in the x direction for jet J1 in the plane $y = -20$ km exceeds 22 m s^{-1} and occurs 50 m above the surface, 50 km before this jet reaches the coast. When jet J1 reaches the sea level, a rapid decrease of the x component of the wind is simulated. It is partly explained by the change in the wind direction in this area and by the turbulent mixing in the katabatic layer. The wind speed decrease is weaker at higher levels (around 100 m above the surface). In fact, the divergence of the turbulent transfer of momentum in these layers is small. This is confirmed by the small variation in the wind norm at these levels downwind over 20 km.

The potential temperature distribution (Fig. 11) shows that in the steepest part of the slope the katabatic layer stratification is in agreement with the observations (see Pettré and André 1991) and consists, from

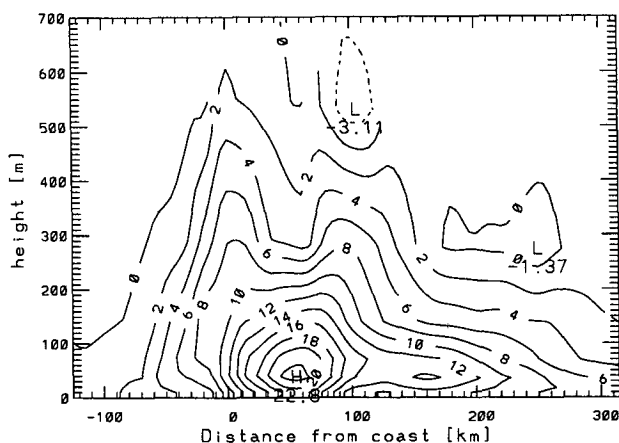


FIG. 10. The x component of the wind field in the plane $y = -20$ km of Fig. 5 after the 36-h time integration, as a function of distance to the coast (positive distances are on the continent) and height above the surface, for simulation N5 (without the Alpert–Neumann correction). Positive values indicate downslope wind and are represented by solid lines. The contour interval is 2 m s^{-1} .

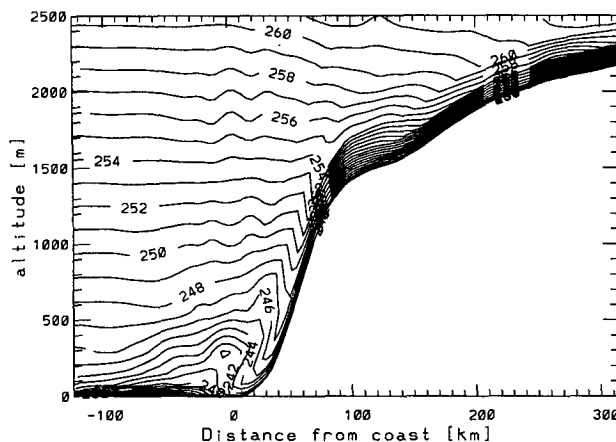


FIG. 11. The potential temperature field in the plane $y = -20$ km of Fig. 5 after the 36-h time integration, as a function of distance to the coast (positive distances are on the continent) and altitude, for simulation N5 (without the Alpert–Neumann correction). The contour interval is 1 K.

the surface upward, in a thin cold-air surface layer, followed by a very stable inversion layer, an unstable layer thickening downslope, and a stable transition layer to the overlying free atmosphere. In the area located near the ice-sheet edge, the model simulates the merging of these katabatic sublayers in one deep layer much colder than the resting air over the ocean. An analysis of the vertical component of the wind (not shown here) indicates that the katabatic flow causes a lifting of cool air in the coastal zone of Terra Nova. The lifting initiates a vertically propagating gravity wave at the coast, as can be seen in Fig. 11. The cold air accumulates in the coastal zone and then flows toward the ocean, causing in this area a cooling of the atmosphere between 100 and 500 m in altitude, at a rate of roughly 10 K day^{-1} .

c. The mesocyclone initiation

As already mentioned, an atmospheric cooling is also simulated by the model over the coastal zone of the Ross Ice Shelf. (See the potential temperature field in Figs. 7 and 8 for the first and fifth sigma levels, respectively.) This cooling is due to advection of katabatic air flowing down over the gentle slope of the Ross Ice Shelf, a situation very comparable to that found in the simulation 2 of Gallée and Schayes (1992). A consequence of the cool katabatic air flowing over the ocean is the formation of two large-scale discontinuities in the potential temperature field, very comparable to boundary-layer fronts. The first one is localized downstream of the Terra Nova valley. The second is localized downstream of the katabatic flow coming from the Ross Ice Shelf. The frontal structures are much weaker above the fifth sigma level, which could be considered the top of the katabatic layer in these

areas. The formation of a minimum in the surface pressure field is associated to the convergence of the frontal structures, as can be seen in Fig. 12. The surface pressure minimum is consistent with the shallow mesocyclones that are observed in the Ross Sea and are inferred to be caused by the katabatic winds (Bromwich 1991). Comparing with the case study discussed by this author, some similarities are found, such as the formation of the mesocyclone during a period of increasing katabatic wind. In the case study, this wind increase corresponds to the increase of the synoptic-scale pressure gradient, while in the model this is simply due to the fact that the simulation starts at rest. The interaction of the mesocyclone with the katabatic flow is evident in both cases, as is shown in the case study by Bromwich (1991, his Fig. 5, p. 1742) and in the model by the streamline pattern (see Fig. 13). Nevertheless, differences exist. Our simulated mesocyclone intensity is 0.4 hPa, while it is an order of magnitude stronger (4 hPa) in the case study. This difference could be partly explained by the fact that the air over the ocean is much warmer in the case study and that its moisture is larger (it was classified as maritime air by Bromwich). Indeed, in our simulation the ocean is covered with ice, while in the case study a moisture source (open water) was located only a few hundred kilometers away over the northwestern Ross Sea, leading to the formation of moist maritime air. Consequently, a significant mesocyclonic activity resulted from a strong temperature discontinuity between the cooler and drier air from the continent and the moist maritime air offshore. Moreover, it should also be mentioned that be-

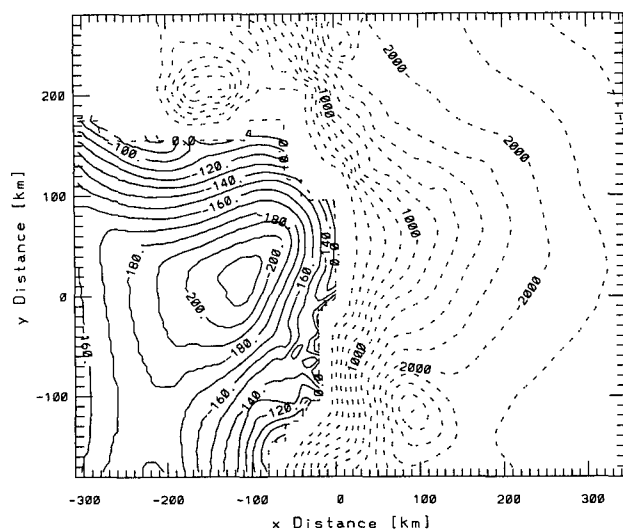


FIG. 12. Model surface pressure anomaly ($p_s - 10^5$ Pa) contours after the 36-h time integration for simulation N5 (without the Alpert–Neumann correction). The surface pressure anomaly has been represented only over the ocean. The contour interval is 10 Pa. Ice-sheet elevation contours (m, dashed) are also plotted. The contour interval is 200 m.

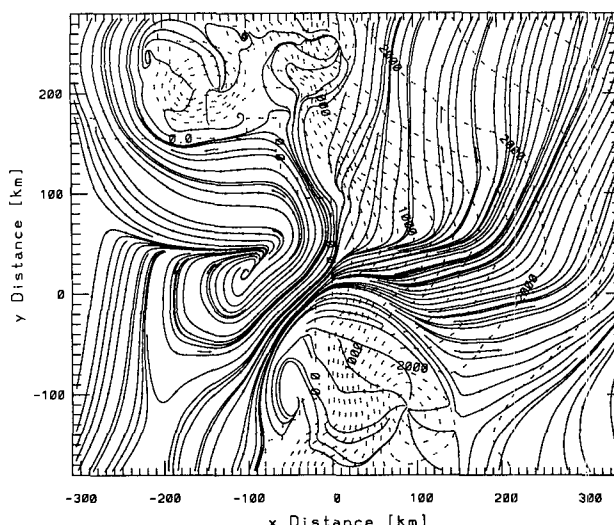


FIG. 13. Model katabatic wind streamlines after the 36-h time integration for the first level of the model (10 m above the surface), for simulation N5 (without the Alpert–Neumann correction). Ice-sheet elevation contours (m, dashed) are also plotted. Contour interval is 200 m.

cause of the large air humidity content, an enhancement of humidity convergence in the boundary-layer front may have resulted, leading to cloud formation, latent heat release, and a subsequent mesocyclone amplification. To confirm the mesocyclone formation process simulated here, further study is thus needed, including a representation of the hydrological cycle, and forcing the model with real synoptic-scale conditions. Finally, the geostrophic forcing observed in the case study causes vortex stretching in the air descending from the high interior of the Antarctic toward the Ross Sea. This could play an important role in mesocyclone generation (Turner et al. 1993).

d. An impact of the topography diffuence

An interesting feature in the lowest sigma level is the decay of the katabatic wind at the left side of the leftmost jet J1 (see Fig. 5). This decay takes place over a short distance. A closer analysis of this decay can be performed by looking at the x component of the wind and the potential temperature distribution in the vertical plane $y = -50$ km of Fig. 5 (see Figs. 14 and 15, respectively). This plane corresponds to a transition zone between confluence and diffuence of the 1000-m surface elevation contour at the left edge of the Terra Nova valley. It is a zone of diffuence for lower surface elevation contours. In the vertical plane $y = -50$ km, the x component of the wind exhibits values larger than 14 m s^{-1} around the 1800-m surface elevation contour. The maximum occurs at the 1100-m surface elevation contour (at $x = 80$ km) but is followed by a sudden decay and even a reversal in the wind direction 50 km

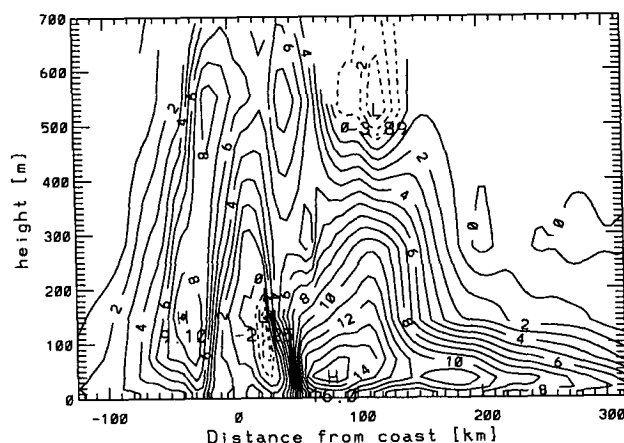


FIG. 14. The x component of the wind field in the plane $y = -50$ km after the 36-h time integration, as a function of distance to the coast (positive distances are on the continent) and height above the surface, for simulation N5 (without the Alpert–Neumann correction). Positive values indicate downslope wind and are represented by solid lines. The contour interval is 1 m s^{-1} .

downstream. The reversal in the wind direction is correlated to upward vertical wind and to the disappearance of the cold-air surface katabatic layer, as already found in the katabatic jump simulated by Gallée and Schayes (1992). In the present simulation, the divergence of cold katabatic air in the diffuence zone could explain a sufficiently large reduction of the sloped-inversion force. Consequently, this force is neutralized by the horizontal pressure gradient generated through the potential temperature discontinuity. (See Fig. 15 in the lower half of the slope.)

e. Discussion

In short, the results of this high-resolution three-dimensional simulation of katabatic wind in the area of Terra Nova Bay compare qualitatively well with those of previous modeling studies. In particular, a katabatic jet is simulated over the bay and the model seems able to initiate circulations generated by katabatic flows, like mesocyclones in the Ross Sea. Nevertheless, the simulated katabatic wind speed is yet underestimated when compared to the observations.

Up to now we do not have a definite explanation about such a shortcoming. There are several possible reasons. The first reason could be the use of a smoothed topography.

Another reason could be that blowing snow, which becomes significant for wind speeds larger than 12 m s^{-1} (e.g., Périard and Pettré 1991) and which contributes substantially to the sloped-inversion force (Kodama et al. 1985) for wind speeds larger than 28 m s^{-1} (Gosink 1989) is not represented in the model.

A third reason could be a too-crude parameterization of turbulence in the model. It has been shown that after

an accelerating phase the katabatic flow shows a closer balance between the pressure gradient force and the stress divergence (“equilibrium flow,” following Mahrt 1982). Entrainment of upper warm air into the katabatic layer plays a key role in the evolution of katabatic wind. When it is overestimated, it could cause the inhibition of the katabatic force.

But it must also be taken into account that the initiation of the model, namely, the initial wind and temperature vertical profile, could impact the katabatic circulation. This possibility has been tested in a sensitivity experiment for which the initial temperature profile has been taken from the zonally averaged mean winter observed conditions at 67°S by Oort (1983). The results show roughly a 10% increase of the wind speed. The impact of the geostrophic wind vector has also been tested, showing an increase of katabatic winds when southerly geostrophic wind prevails.

The polynya that is not represented in the simulation could also impact the katabatic flow, because the surface temperature would be considerably higher there, (271.2 K , seawater freezing temperature) giving rise to a “land breeze” effect that could strengthen the katabatic wind.

5. Conclusions

The aim of the present work is to develop a three-dimensional mesoscale atmospheric model in order to simulate strong katabatic flow in highly complex terrain. In particular, it must be a useful tool for the study of the processes governing the katabatic wind evolution in Antarctic coastal zones, like in the Terra Nova Bay area. The primitive equations are used, including the full continuity equation. A correction to get horizontal subgrid-scale fluxes is added (the Alpert–Neumann

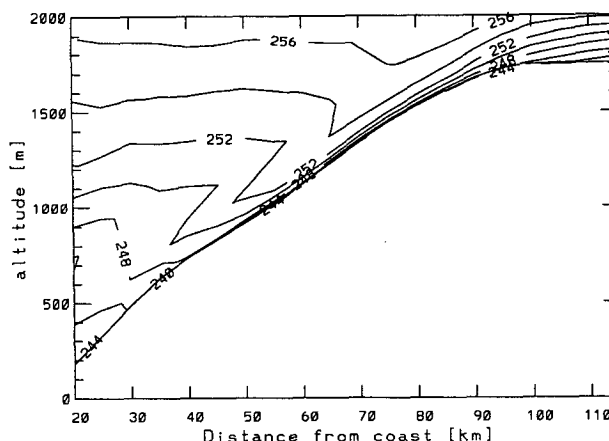


FIG. 15. The potential temperature field in the plane $y = -50$ km after the 36-h time integration, as a function of distance to the coast (positive distances are on the continent) and altitude, for simulation N5 (without the Alpert–Neumann correction). The contour interval is 2 K .

correction). The vertical turbulent fluxes are parameterized using a first-order closure scheme.

The model is validated by performing the classical linear mountain wave experiments. The simulated linear waves are similar to those found in the analytical solution of the equations. The linear response of the model is numerically very stable, which is of particular importance for the simulation of drainage flows, because excessive numerical damping is prohibited.

Then a simulation of katabatic wind is performed for polar night conditions in the area of Terra Nova Bay. The horizontal resolution is tested and the model converges for grid sizes smaller or equal to 10 km. For the 5-km resolution, the model is not sensitive to the use of the Alpert–Neumann correction.

The simulated fields reproduce many characteristics of the observed katabatic flow in the Terra Nova Bay area. Katabatic jets are simulated in agreement with the observations. Moreover, the advance of the cold katabatic flow over the ocean causes the formation of boundary-layer fronts and of an associated mesocyclone. The simulated mesocyclone does not exhibit comparable strength with the observed ones but similarities exist.

Despite the qualitative agreement with the observations, the simulated katabatic winds are not sufficiently strong and could be improved at least by using a more sophisticated parameterization of turbulence and by including additional processes like the increase of the negative buoyancy of the katabatic layer due to the presence of blowing snow.

Finally, the model is a useful tool for the study of ocean–atmosphere–ice-sheet interactions at short time scales and could help a lot to understand the climate of an ice sheet and its surroundings. This is of particular importance because of the major role played by ice sheets in the climate system.

Acknowledgments. This research is sponsored by the Belgian Program “Scientific Research on the Antarctic” (Services of the Prime Minister—Science Policy Office) under Contract ANTAR03. The authors wish to thank the thoughtful comments made by the three reviewers of the *Monthly Weather Review*. We also thank Dr. P. Alpert for useful discussions and comments. The authors acknowledge Prof. A. Berger and Dr. J. P. van Ypersele for continued support.

REFERENCES

- Alpert, P., and J. Neumann, 1984: On the enhanced smoothing over topography in some mesometeorological models. *Bound.-Layer Meteor.*, **30**, 293–312.
- , A. Cohen, J. Neumann, and E. Doron, 1982: A model simulation of the summer circulation from the eastern Mediterranean past Lake Kinneret in the Jordan Valley. *Mon. Wea. Rev.*, **110**, 994–1006.
- André, J.-Cl., G. Wendler, and M. Zéphoris, 1986: The “IAGO–Katabatic” Programme. *Antarct. Climate Res.*, **1**, 17–18.
- Baldi, M., A. Di Menno, A. Guerrini, A. Anav, M. Di Menno, and C. Valenti, 1990: Climatology analysis in the boundary layer at Terra Nova Bay, Antarctica. *Italian Research on Antarctic Atmosphere, Second Workshop*, M. Colacino, G. Giovannelli, and L. Stefanutti, Eds., Società Italiana di Fisica, 121–140.
- Bromwich, D. H., 1989a: Satellite analyses of Antarctic katabatic wind behavior. *Bull. Amer. Meteor. Soc.*, **70**, 738–749.
- , 1989b: An extraordinary katabatic wind regime at Terra Nova Bay, Antarctica. *Mon. Wea. Rev.*, **117**, 688–695.
- , 1991: Mesoscale cyclogenesis over the southwestern Ross Sea linked to strong katabatic winds. *Mon. Wea. Rev.*, **119**, 1736–1752.
- , and D. D. Kurtz, 1984: Katabatic wind forcing of the Terra Nova Bay polynia. *J. Geophys. Res.*, **89**, 3561–3572.
- , T. R. Parish, and C. A. Zorman, 1990: The confluence zone of the intense katabatic winds at Terra Nova Bay, Antarctica, as derived from airborne sastrugi surveys and mesoscale numerical modeling. *J. Geophys. Res.*, **95**, 5495–5509.
- Businger, J. A., 1973: Turbulent transfer in the atmospheric surface layer. *Workshop on Micrometeorology*, Amer. Meteor. Soc., 67–100.
- Deardorff, J. W., 1978: Efficient prediction of ground surface temperature and moisture with inclusion of a layer of vegetation. *J. Geophys. Res.*, **83**, 1889–1903.
- Drewry, D. J., 1983: The surface of the Antarctic ice sheet, *Antarctica: Glaciological and Geophysical Folio*, Sheet 2, D. J. Drewry, Ed., Scott Polar Research Institute, University of Cambridge.
- Gallée, H., and G. Schayes, 1992: Dynamical aspects of katabatic winds evolution in the Antarctic coastal zone. *Bound.-Layer Meteor.*, **59**, 141–161.
- , A. Berger, G. Schayes, Th. Fichet, I. Marsiat, C. Tricot, and J.-P. van Ypersele, 1989: Numerical study of the air sea interactions in the Antarctic coastal zone and their implications on deep sea formation in the case of katabatic winds. *Belgian Scientific Research Programme on Antarctica, Scientific Results of Phase One (Oct 85–Jan 89)*, vol. III, S. Caschetto, Ed., Prime Minister’s Services, Science Policy Office, Brussels, III-1–III-40.
- Gordon, A. L., 1988: The southern ocean and global climate. *Oceanus*, **31**, 2, 39–46.
- Gosink, J. P., 1989: The extension of a density current model of katabatic winds to include the effects of blowing snow and sublimation. *Bound.-Layer Meteor.*, **49**, 367–394.
- Klemp, J. B., and D. K. Lilly, 1978: Numerical simulation of hydrostatic waves. *J. Atmos. Sci.*, **35**, 78–107.
- Kodama, Y., and G. Wendler, 1986: Wind and temperature regime along the slope of Adélie Land, Antarctica. *J. Geophys. Res.*, **91**, 6735–6741.
- , —, and J. Gosink, 1985: The effect of blowing snow on katabatic winds in Antarctica. *Ann. Glaciol.*, **6**, 59–62.
- Kurtz, D. D., and D. H. Bromwich, 1985: A recurring, atmospherically forced polynia in Terra Nova Bay. *Oceanology of the Antarctic Continental Shelf. Antarct. Res. Series*, **43**, 177–201.
- Long, P. E., W. A. Shaffer, J. E. Kemper, and F. J. Hicks, 1978: The state of the techniques development laboratory’s boundary layer model. NOAA Tech. Memo. NWS TDL66, Silver Spring, MD, 63 pp.
- Louis, J.-F., 1979: A parametric model of vertical eddy fluxes in the atmosphere. *Bound.-Layer Meteor.*, **17**, 187–202.
- Mahrer, Y., and R. A. Pielke, 1978: A test of an upstream spline interpolation technique for the advective terms in a numerical mesoscale model. *Mon. Wea. Rev.*, **106**, 818–830.
- Mahrt, L., 1982: Momentum balance of gravity flows. *J. Atmos. Sci.*, **39**, 2701–2711.
- Marchuk, G. I., 1974: *Numerical Methods in Weather Prediction*. Academic Press, 277 pp.
- Mather, K. B., and G. S. Miller, 1967: Notes on topographic factors affecting the surface wind in Antarctica, with special reference to katabatic winds, and bibliography. Tech. Rep. of the University of Alaska, 63 pp.
- Miller, M. J., and A. J. Thorpe, 1981: Radiation conditions for the lateral boundaries of limited area numerical models. *Quart. J. Roy. Meteor. Soc.*, **107**, 615–628.

- Orlanski, I., 1976: A simple boundary condition for unbounded hyperbolic flows. *J. Comput. Phys.*, **21**, 251–269.
- Parish, T. R., 1984: A numerical study of strong katabatic winds over Antarctica. *Mon. Wea. Rev.*, **112**, 545–554.
- , 1988: Surface winds over the Antarctic continent: A review. *Rev. Geophys.*, **26**, 169–180.
- , and D. H. Bromwich, 1987: The surface wind field over the Antarctic ice sheets. *Nature*, **328**, 51–54.
- , and —, 1989: Instrumented aircraft observations of the katabatic wind regime near Terra Nova Bay. *Mon. Wea. Rev.*, **117**, 1570–1585.
- , and —, 1991: Continental-scale simulation of the Antarctic katabatic wind regime. *J. Climate*, **4**, 135–145.
- Pease, C. H., 1987: The size of wind-driven coastal polynyas. *J. Geophys. Res.*, **92**, 7049–7059.
- Périard, Ch., and Pettré, P., 1991: Climatologie de Dumont d'Urville, Terre Adélie, Antarctique, *Volume d'Actes de l'Atelier de Modélisation de l'Atmosphère*, Météo-France/C.N.R.M./P.A.D., Toulouse, 99–109.
- Pettré, P., and J.-Cl. André, 1991: Surface-pressure change through Loewe's phenomena and katabatic flow jumps: Study of two cases in Adélie Land, Antarctica. *J. Atmos. Sci.*, **48**, 557–571.
- Pielke, R. A., 1984: *Mesoscale Meteorological Modeling*. Academic Press, 612 pp.
- Purser, R. J., and L. M. Leslie, 1988: A semi-implicit, semi-Lagrangian finite-difference scheme using high-order spatial differencing on a non-staggered grid. *Mon. Wea. Rev.*, **116**, 2069–2080.
- Queney, P., 1948: The problem of airflows over mountains: A summary of theoretical studies. *Bull. Amer. Meteor. Soc.*, **29**, 16–26.
- Raymond, W. H., and A. Garder, 1988: A spatial filter for use in finite area calculations. *Mon. Wea. Rev.*, **116**, 209–222.
- Sasamori, T., 1968: The radiative calculation for application to general circulations experiments. *J. Appl. Meteor.*, **7**, 721–729.
- Schwerdtfeger, W., 1984: Weather and climate of the antarctic. *Developments in Atmospheric Sciences*, No. 15, Elsevier, 261 pp.
- Seibert, P., and B. Morariu, 1991: Improvements of upstream, semi-lagrangian numerical advection schemes. *J. Appl. Meteor.*, **30**, 117–125.
- Smagorinsky, J. S., 1963: General circulation experiments with the primitive equations: I. The basic experiment. *Mon. Wea. Rev.*, **91**, 99–164.
- Tag, P. M., F. W. Murray, and R. Koenig, 1979: A comparison of several forms of eddy viscosity parameterization in a two-dimensional cloud model. *J. Appl. Meteor.*, **18**, 1429–1441.
- Turner, J., T. A. Lachlan-Cope, D. E. Warren, and C. N. Duncan, 1993: A mesoscale vortex over Halley Station, Antarctica. *Mon. Wea. Rev.*, **121**, 1317–1336.
- Wendler, G., Y. Kodama, and A. Poggi, 1983: Katabatic wind in Adélie Land. *Antarct. J. U.S.*, **18**, 236–238.
- Yan, H., and R. A. Anthes, 1987: The effect of latitude on the sea breeze. *Mon. Wea. Rev.*, **115**, 937–956.
- Zwally, H. J., J. C. Comiso, and A. L. Gordon, 1985: Antarctic offshore leads and polynyas and oceanographic effects. *Oceanology of the Antarctic Continental Shelf. Antarct. Res. Series*, **43**, 203–226.